

# Electronic structure and magnetic properties in $T_2\text{AlB}_2$ ( $T = \text{Fe, Mn, Cr, Co, and Ni}$ ) and their alloys

Liqin Ke,<sup>1,\*</sup> Bruce N. Harmon,<sup>1</sup> and Matthew J. Kramer<sup>1</sup>

<sup>1</sup>*Ames Laboratory, U.S. DOE, Ames, Iowa 50011, USA*

(Dated: July 10, 2018)

The electronic structure and intrinsic magnetic properties of  $\text{Fe}_2\text{AlB}_2$ -related compounds and their alloys have been investigated using density functional theory. For  $\text{Fe}_2\text{AlB}_2$ , the crystallographic  $a$  axis is the easiest axis, which agrees with experiments. The magnetic ground state of  $\text{Mn}_2\text{AlB}_2$  is found to be ferromagnetic in the basal  $ab$  plane, but antiferromagnetic along the  $c$  axis. All  $3d$  dopings considered decrease the magnetization and Curie temperature in  $\text{Fe}_2\text{AlB}_2$ . Electron doping with Co or Ni has a stronger effect on the decreasing of Curie temperature in  $\text{Fe}_2\text{AlB}_2$  than hole doping with Mn or Cr. However, a larger amount of Mn doping on  $\text{Fe}_2\text{AlB}_2$  promotes the ferromagnetic to antiferromagnetic transition. A very anisotropic magnetoelastic effect is found in  $\text{Fe}_2\text{AlB}_2$ : the magnetization has a much stronger dependence on the lattice parameter  $c$  than on  $a$  or  $b$ , which is explained by electronic-structure features near the Fermi level. Dopings of other elements on B and Al sites are also discussed.

## I. INTRODUCTION

Magnetic cooling, which is based on the magnetocaloric effect (MCE) and was discovered one century ago, has long been used in scientific laboratories to attain extremely low temperatures. A major breakthrough came in the late 1990s when Pecharsky and Gschneidner discovered giant MCE around room temperature (RT) in a new class of magnetic materials [1]. This discovery has rekindled research interest in utilizing MCE for much broader applications, such as domestic appliances, which usually operate around RT. If successful, this more energy-efficient and environment-friendly magnetic cooling technique may replace conventional compressor-based refrigeration and revolutionize the cooling industry. This new era may arrive in the near future—only if one can find or engineer a proper MCE material which has large MCE under a magnetic field that can be generated by permanent magnets, and is also abundant, affordable, and has a good lifespan.

$\text{Fe}_2\text{AlB}_2$  is one of the promising candidates for this purpose and has attracted great attention since the recent discovery of its substantial MCE around RT [2]. The reported entropy change has a value of  $\Delta S_m = 4.1\text{--}7.7 \text{ J kg}^{-1} \text{ K}^{-1}$  in the presence of an external field  $B = 2\text{--}5 \text{ T}$ . Although  $\text{Fe}_2\text{AlB}_2$  does not have the largest MCE of all materials, it does not contain any rare, expensive, or toxic elements. Moreover, its volume barely changes during the magnetic transition [3], which may ensure  $\text{Fe}_2\text{AlB}_2$  has a good life span for refrigerator applications operating at high cycle frequencies [4, 5].

The MCE often peaks at the Curie temperature  $T_C$  of the material; however, real applications require materials with a large MCE over a certain operating temperature range. This likely needs to be achieved by using composite materials with multiple compositions, so the

system can have MCE over the whole operating temperature range for specific applications. It seems the first logical selection of doping would be the substitution of Fe with other  $3d$  transition-metal elements  $T$ . Pure  $\text{Mn}_2\text{AlB}_2$  [6] and  $\text{Cr}_2\text{AlB}_2$  [7] can be formed and share the same structure of  $\text{Fe}_2\text{AlB}_2$ . Combining theory with experiments, Kádas *et al.* studied the phase stability in  $T_2\text{AlB}_2$  with  $T = \text{Cr, Mn, Fe, Co, and Ni}$ . They found that although compounds are metastable with  $T = \text{Co and Ni}$ ,  $\text{Fe}_{2-x}\text{Co}_x\text{AlB}_2$ ,  $\text{Fe}_{2-x}\text{Ni}_x\text{AlB}_2$ , or even  $(\text{Fe}_{2-x-y}\text{Co}_x\text{Ni}_y)\text{AlB}_2$  could be stable [8]. However, the magnetic properties of those alloys or even their parent compounds are not well understood. For example, the magnetic ground state of  $\text{Mn}_2\text{AlB}_2$  had been reported to be ferromagnetic (FM) [6], but recent experiments concluded that it should be either nonmagnetic (NM) or antiferromagnetic (AFM) [9]. To provide guidance on tuning  $\text{Fe}_2\text{AlB}_2$ , a better understanding of the magnetic properties of pure  $T_2\text{AlB}_2$  and their alloys is desired.

The high melting temperature of FeB makes it a difficult impurity to remove from  $\text{Fe}_2\text{AlB}_2$  samples. The rapid cooling by melt spinning had been used to greatly improve the  $\text{Fe}_2\text{AlB}_2$  purity by suppressing the growth of FeB [4]. On the other hand, extra Al is often added during the synthesis to decrease the formation of FeB impurities [4, 10]. With a higher Al content,  $\text{Al}_{13}\text{Fe}_4$  becomes the main impurity phase. Reported magnetization values measured at low temperature vary between  $1.0$  and  $1.32 \mu_B/\text{Fe}$  and the  $T_C$  values vary between  $282$  and  $320 \text{ K}$  [2, 4, 9, 11]. The variation of experimental values may be due to the existence of an impurity phase in the  $\text{Fe}_2\text{AlB}_2$  sample.

Experimentally, substitution of Mn [4, 5, 9] or up to  $15\%$  of Co [10] on Fe sites had been reported; a large amount of Mn or Co doping makes the structures unstable [4] or phase inhomogeneous [9]. Both dopings decrease the magnetization and  $T_C$  in  $\text{Fe}_2\text{AlB}_2$ . A spin-glass state had been found in  $\text{Fe}_{1.5}\text{Mn}_{0.5}\text{AlB}_2$  at low temperature [5]. With Co doping,  $T_C$  and the Co content are

\* Corresponding author: liqinke@ameslab.gov

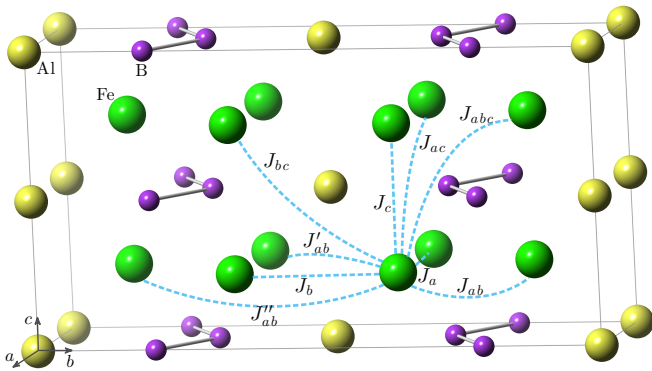


FIG. 1. Schematic representation of the crystal structure of  $\text{Fe}_2\text{AlB}_2$ . The conventional cell is doubled along the  $c$  axis to depict pair exchange parameters for the first few neighbors of Fe atoms (large green spheres). Al atoms are indicated with yellow spheres. B atoms, indicated by small purple spheres, form zigzag chains along the  $a$  axis. Exchange parameters are labeled according to the axis or plane of the connecting vector.

linearly correlated, which makes Co content a convenient parameter to tune the material to have MCE between RT and 200 K [10]. A few studies have been reported to investigate the electronic structures and structural, electronic, and magnetic properties of  $\text{T}_2\text{AlB}_2$  [9, 11–13].

In this work, using density functional theory (DFT), we investigate the intrinsic magnetic properties including magnetization, exchange parameters, Curie temperature, and magnetocrystalline anisotropy in  $\text{T}_2\text{AlB}_2$  and their alloys. The magnetoelastic effect in  $\text{Fe}_2\text{AlB}_2$  and the dopings of various elements on B and Al sites are also discussed. Electronic structures are studied to understand the magnetic properties.

## II. COMPUTATIONAL DETAILS

### A. Crystal structure

$\text{Fe}_2\text{AlB}_2$  crystallizes in the orthorhombic  $\text{Mn}_2\text{AlB}_2$ -type ( $Cmmm$ , space group no. 65) structure. The primitive cell contains one formula unit (f.u.) while the conventional cell contains two. The crystal structure is shown in Fig. 1. We double the conventional cell along the  $c$  axis to denote the first few exchange parameters. B atoms occupy the  $4i(m2m)$  site, forming a zigzag chain in the  $ab$  plane and along the  $a$  axis. Fe atoms occupy the  $4j(m2m)$  sites and form  $\text{Fe}_6\text{B}$  prisms with neighboring B atoms. The structure can be derived from the  $\text{FeB}$  structure by inserting one layer of Al atoms perpendicular to the  $b$  axis, between each pair of planes containing the  $\text{Fe}_6\text{B}$  prisms [14]. Each Al atom, which occupies the  $2a(mmm)$  site, is surrounded by eight Fe atoms. Together they form a body-centered-tetragonal cell elongated along the  $b$  axis. For this Fe-Al cage, the Fe-Al bond length is 2.61 Å and the Fe-Fe distances are 2.87,

2.92, and 3.22 Å, along the  $c$ ,  $a$ , and  $b$  directions, respectively. Lying in the  $ab$  plane, the nearest Fe-Fe bond has a length of 2.72 Å. The structure can also be derived by stacking the pure Fe plane and the Al-B plane alternatively along the  $c$  axis. This view is probably more convenient to understand the magnetic properties, such as exchange coupling and magnetoelastic effect, both of which are very anisotropic, behaving very differently along the  $c$  axis than along the  $a$  or  $b$  axis, as we will discuss later.

### B. Computational methods

Electronic structure and most magnetic properties are calculated using a standard linear muffin-tin orbital (LMTO) basis set [15] generalized to full potentials (FP) [16]. This scheme employs generalized Hankel functions as the envelope functions. Calculations are carried out within the generalized gradient approximation (GGA) to DFT with the exchange-correlation parametrization of Perdew, Burke, and Ernzerhof (PBE) [17], unless LDA [18] (local density approximation, with the exchange-correlation parametrization of von Barth and Hedin) is specified.

The magnetocrystalline anisotropy energy (MAE) is calculated using the force theorem [19]. Starting from the self-consistent scalar-relativistic potential, the spin-orbit coupling (SOC) is included in a subsequent one-step calculation with spin being along direction  $\hat{\mathbf{n}}$ . The MAE is characterized below as  $K_{\hat{\mathbf{n}}} = E_{\hat{\mathbf{n}}} - E_{001}$ , where  $E_{001}$  and  $E_{\hat{\mathbf{n}}}$  are the summation of occupied band energies for the magnetization being oriented along the  $[001]$  and  $\hat{\mathbf{n}}$  directions, respectively.

Exchange coupling parameters  $J_{ij}$  are calculated using a static linear-response approach implemented in a Green's function (GF) LMTO method, simplified using the atomic sphere approximation (ASA) to the potential and density [20, 21]. The scalar-relativistic Hamiltonian is used so SOC is not included, although it is a small perturbation on  $J_{ij}$ 's. In the basis set,  $s, p, d$  orbitals are included for T and Al atoms, and  $s, p$  orbitals are included for the B atom. A dense  $k$ -point mesh is used to calculate exchange parameters  $J(\mathbf{q})$ , e.g., a  $32^3$   $k$ -point mesh for the five-atom cell. The real-space  $J(\mathbf{R})$  are obtained by a subsequent Fourier transform. Curie temperatures are estimated in the mean-field approximation (MFA) with  $k_B T_C = 2/3 \sum_i J_{0i}$ . The coherent potential approximation (CPA) implemented within the LMTO-ASA-GF code is used to address the chemical effects of doping on magnetization and  $T_C$ . Without using supercell calculations, the CPA provides an elegant and efficient approach to investigate substitutional effects with an arbitrary composition. The details of the methods and applications can be found elsewhere [21, 22].

Both experimental and theoretically optimized crystal structures are used to investigate the magnetic properties. We fully relax internal atomic positions and lattice constants with the PBE functional using a fast

TABLE I. Calculated atomic spin magnetic  $m_i$ , spin magnetization  $M$ , and Curie temperature  $T_C$  in  $\text{Fe}_2\text{AlB}_2$ .

$\text{Fe}_2\text{AlB}_2$ Method	$m_i$ ( $\mu_B/\text{atom}$ )			$M$ ( $\mu_B/\text{f.u.}$ )	$T_C$ (K)
	Fe	Al	B		
FP-GGA	1.43	-0.04	-0.01	2.73	
ASA-GGA	1.38	-0.08	-0.04	2.62	329
FP-LDA	1.31	-0.01	-0.03	2.54	
ASA-LDA	1.20	-0.06	-0.03	2.29	232

plane-wave method, as implemented within the Vienna *ab initio* simulation package (VASP) [23, 24]. The nuclei and core electrons are described by the projector augmented-wave potential [25] and the wave functions of valence electrons are expanded in a plane-wave basis set with a cutoff energy of up to 520 eV.

### III. RESULTS AND DISCUSSION

#### A. Pure compounds: Exchange coupling, magnetic anisotropy, and spin configurations

Table I shows the atomic spin moments  $m_i$  at each sublattice and magnetization  $M$  in  $\text{Fe}_2\text{AlB}_2$ , which are calculated using the experimental lattice constants and atomic position parameters from Ref. [26]. Al and B have small moments antiparallel to the Fe sublattice. Within the GGA, a magnetization of  $M = 1.36 \mu_B/\text{Fe}$  is obtained using FP. For the sake of comparison, we carry out similar calculation for the parent compound, FeB, and obtain a magnetization of  $M = 1.20 \mu_B/\text{Fe}$ . The smaller Fe moment in FeB is likely due to its smaller Fe-Fe bond length (2.62 Å) than in  $\text{Fe}_2\text{AlB}_2$ . ASA gives a slightly smaller (by 4%) magnetization than FP in  $\text{Fe}_2\text{AlB}_2$ , suggesting that ASA is suitable for this material. The calculated  $T_C = 329$  K is slightly above the upper bound of the reported experimental  $T_C$  values. The agreement is fair considering the MFA generally overestimates  $T_C$ . LDA gives smaller magnetization, especially with ASA, resulting in a smaller  $T_C$ .

Starting from the FM configuration and using experimental crystal structures, we calculate the exchange coupling  $J_{ij}$  in  $\text{Fe}_2\text{AlB}_2$  and  $\text{Mn}_2\text{AlB}_2$ . Figure 2 shows the  $J_{ij}$  as a function of the distance  $R_{ij}$ . In both compounds  $J_{ij}$  becomes negligible after  $R_{ij} > 6$  Å. The exchange parameters between the first few nearest neighbors are also listed in Table II. Here,  $J_{ij}$  can be treated as stability parameters and a negative  $J_{ij}$  indicates that the given spin configuration is not favorable for that particular pair of sites [21].

For  $\text{Fe}_2\text{AlB}_2$ , all of the first four nearest exchange parameters are positive. The  $J_{ij}$  value increases with distance, reaching maximum at  $J_b$ , and then decrease, which generally agrees with the previous study [13]. LDA gives a similar trend but a smaller amplitude of  $J_{ij}$  than GGA,

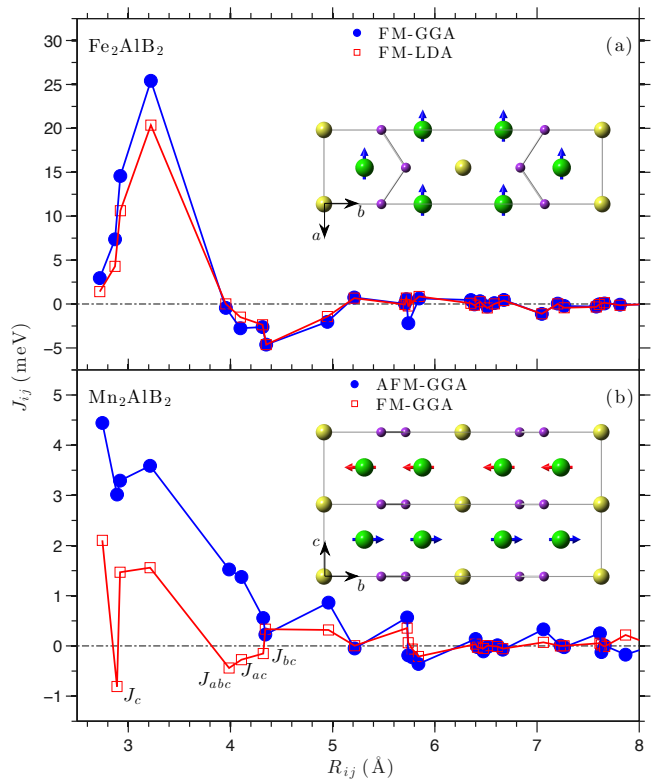


FIG. 2. Real-space magnetic exchange parameters  $J_{ij}$  in  $\text{Fe}_2\text{AlB}_2$  (a), and  $\text{Mn}_2\text{AlB}_2$  (b) as functions of distance. For  $\text{Fe}_2\text{AlB}_2$ , both GGA and LDA results are shown. For  $\text{Mn}_2\text{AlB}_2$ , both FM and AFM spin configurations are calculated within GGA. The spin configurations of their magnetic ground states are shown in the insets.

which reflects the smaller magnetic moments obtained within LDA.

The magnetic ground state of  $\text{Mn}_2\text{AlB}_2$  is not well understood [9]. For simplicity, we start from the FM configuration. The calculated magnetization is  $0.42 \mu_B/\text{Mn}$ , which agrees well with a previous FM calculation [9]. Exchange parameters calculated in the FM configuration show a very interesting feature: all dominant  $J_{ij}$  are positive for neighbors within the Mn *ab* plane but negative for neighbors between neighboring Mn layers, namely,  $J_c$ ,  $J_{abc}$ ,  $J_{ac}$ , and  $J_{bc}$ . This suggests that the FM coupling of Mn atoms is stable within the *ab* layer but not between neighboring layers. To confirm it, we calculate  $J_{ij}$  for the AFM configuration, in which FM Mn *ab* layers couple antiferromagnetically along the *c* axis. This AFM configuration gives lower energy than the FM configuration. Moreover, as shown in Fig. 2(b), the dominant exchange parameters become all positive and larger. To better quantify the relative stability of those two spin configurations, we fully relaxed the structure and found that the AFM configuration increases the on-site Mn moment to  $0.75 \mu_B/\text{Mn}$  and lowers the total energy by 42 meV/f.u. Unlike  $\text{Fe}_2\text{AlB}_2$ , the largest exchange interaction in  $\text{Mn}_2\text{AlB}_2$  is  $J_{ab}$ , which is between

TABLE II. Pairwise exchange parameters  $J_{ij}$  for the Heisenberg Hamiltonian  $H = -\sum J_{ij} \hat{\mathbf{e}}_i \cdot \hat{\mathbf{e}}_j$ , and  $\hat{\mathbf{e}}_i$  is the unit vector pointing along the direction of the local spin moment at site  $i$ . The experimental lattice parameters and atomic positions are used. For  $\text{Fe}_2\text{AlB}_2$ , both GGA and LDA results are shown. For  $\text{Mn}_2\text{AlB}_2$ , the PBE functional is used, and both FM and AFM spin configurations are considered.

$\text{Fe}_2\text{AlB}_2$		$R_{ij}$		$\hat{\mathbf{R}}_{ij}$			$J_{ij}(\text{meV})$	
Lbl.	No.	(Å)	(a)	$x$	$y$	$z$	GGA	LDA
$J_{ab}$	2	2.721	0.931	0.5	0.785	0	2.95	1.41
$J_c$	2	2.870	0.982	0	0	0.982	7.36	4.29
$J_a$	2	2.923	1	1	0	0	14.58	10.63
$J_b$	1	3.222	1.102	0	1.102	0	25.41	20.37
$J_{abc}$	4	3.955	1.353	0.5	-0.785	0.982	-0.43	0.01
$J_{ac}$	4	4.097	1.401	1	0	0.982	-2.76	-1.49
$J_{bc}$	2	4.315	1.476	0	1.102	0.982	-2.63	-2.37
$J'_{ab}$	2	4.350	1.488	1	1.102	0	-4.62	-4.62
$J''_{ab}$	2	4.949	1.693	1.5	-0.785	0	-2.03	-1.43

$\text{Mn}_2\text{AlB}_2$		$R_{ij}$		$\hat{\mathbf{R}}_{ij}$			$J_{ij}(\text{meV})$	
Lbl.	No.	(Å)	(a)	$x$	$y$	$z$	FM	AFM
$J_{ab}$	2	2.747	0.941	0.5	-0.797	0	2.10	4.44
$J_c$	2	2.890	0.990	0	0	-0.990	-0.81	3.02
$J_a$	2	2.920	1	1	0	0	1.47	3.29
$J_b$	1	3.213	1.100	0	1.100	0	1.56	3.59
$J_{abc}$	4	3.987	1.365	-0.5	-0.797	0.990	-0.44	1.52
$J_{ac}$	4	4.108	1.407	-1	0	0.990	-0.27	1.37
$J_{bc}$	2	4.322	1.480	0	1.100	0.990	-0.15	0.56
$J'_{ab}$	2	4.342	1.487	-1	1.100	0	0.33	0.23
$J''_{ab}$	2	4.960	1.698	-1.5	-0.797	0	0.32	0.86

the nearest Mn neighbors. The Néel temperature is estimated to be  $T_N = 310\text{K}$  within MFA for the AFM configuration with the experimental crystal structure.

Next we consider the SOC effect in  $\text{Fe}_2\text{AlB}_2$ . Figure 3 shows the energy and the average orbital magnetic moments of each sublattice as functions of spin quantization axis orientation, which rotates from the  $c \rightarrow a \rightarrow b \rightarrow c$  axis. The relaxed structure was used for the calculations. The  $a$  axis is the easiest axis, which agrees with recent neutron scattering experiments [13]. The  $c$  axis is the hardest axis, while the anisotropy within the  $ab$  plane is very small. Energy changes by  $K_{100} = -0.38\text{meV/f.u.}$  ( $-1.34\text{MJ/m}^3$ ) when the spin quantization axis rotates from the  $c$  axis to the  $a$  axis. The anisotropy calculated using experimental structure [26] is larger by  $\sim 10\%$ , reaching  $K_{100} = -1.47\text{MJ/m}^3$ . B and Al atoms have negligible orbital magnetic moments, as expected for light  $2p$  and  $3p$  elements. The orbital moment of Fe is also rather small, and interestingly has the largest value of  $0.02\mu_B/\text{Fe}$  when spin is along the hardest  $c$  axis instead of in the  $ab$  plane. Similar behavior has also been found in materials such as FePt [27]. To elucidate the origin of MAE, we evaluate the anisotropy of the on-site SOC energy with respect to the  $c$  axis and the  $ab$  plane,  $K_{110}^{\text{so}} = \frac{1}{2}\langle V_{\text{so}} \rangle_{110} - \frac{1}{2}\langle V_{\text{so}} \rangle_{001}$ , and resolve it into four spin channels [28, 29]. It is well known that only when the MAE is dominated by the  $\downarrow\downarrow$  term, one may

expect an obvious correlation between the orbital moment and MAE, and a larger orbital moment along the easy axis [28, 30]. As shown in the inset of Fig. 3(b), the amplitudes of four spin components of  $K_{\text{so}}^{\sigma\sigma'}$  are comparable. The  $\downarrow\downarrow$  term favors the spin to be along the  $c$  axis, while the other three terms ( $\uparrow\uparrow$ ,  $\uparrow\downarrow$ , and  $\downarrow\uparrow$ ) favor the spin to lie in the  $ab$  plane, explaining the absence of the correlation between MAE and orbital moment in  $\text{Fe}_2\text{AlB}_2$ . LDA gives a smaller anisotropy ( $K_{100} = -0.82\text{MJ/m}^3$  using experimental structure) but a similar trend of angular dependence of energy. For  $\text{Mn}_2\text{AlB}_2$ , the  $c$  axis is also the hardest axis. Within the  $ab$  plane, the system has slightly lower energy when the spin is along the  $b$  axis. As expected, its anisotropy is much smaller than in  $\text{Fe}_2\text{AlB}_2$ . The schematic representation of the ground-state spin configurations of  $\text{Fe}_2\text{AlB}_2$  and  $\text{Mn}_2\text{AlB}_2$  are shown in the insets of Fig. 2.

Figure 4 shows the scalar-relativistic partial density of states (PDOS) projected on individual elements in  $T_2\text{AlB}_2$  with  $T = \text{Cr, Mn, Fe, Co, and Ni}$ . The total density of states (DOS), scaled by 1/2, is also shown to compare. The total DOS of  $\text{Fe}_2\text{AlB}_2$  compares well with previously reported calculations [9]. Al-3s and B-2s states are located between  $-12$  and  $-7\text{eV}$  below the Fermi level  $E_F$ . Al-3p states hybridize with  $T$  atoms at around  $-4\text{eV}$  below  $E_F$ . For  $\text{Mn}_2\text{AlB}_2$ , the Fermi level is located at a pseudogap in the AFM configuration, and the DOS at

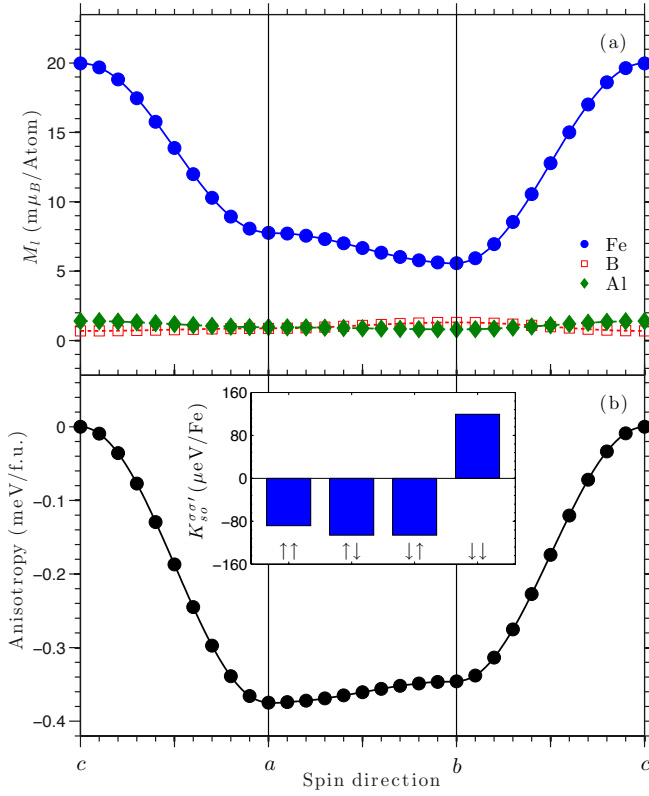


FIG. 3. Variation of (a) atomic orbital magnetic moments of Fe, Al, and B sublattices, and (b) energy as functions of spin quantization axis rotation in  $\text{Fe}_2\text{AlB}_2$ . The inset in panel (b) shows the spin-resolved anisotropy of Fe-site spin-orbit coupling energy  $K_{so}^{\sigma\sigma'} = \frac{1}{2}\langle V_{so} \rangle_{110} - \frac{1}{2}\langle V_{so} \rangle_{001}$ .

$E_F$  is smaller than in the FM configuration, which again suggests that the AFM configuration is more stable. The calculated hypothetical  $\text{Co}_2\text{AlB}_2$  shows a weak magnetic moment of about  $0.2 \mu_B/\text{Co}$ . The two peaks at  $\pm 0.1 \text{ eV}$  around the Fermi level, as shown in Fig. 4(d), will be pinched at  $E_F$  in the non-spin-polarized calculation (not shown). Thus, the small spin polarization decreases the DOS at  $E_F$  and stabilizes the system. The calculated  $\text{Cr}_2\text{AlB}_2$  and hypothetical  $\text{Ni}_2\text{AlB}_2$  are nonmagnetic and have small DOS at  $E_F$ . It is worth noting that  $\text{Ni}_x\text{B}_{1-x}$  systems become magnetic only after  $x > 0.75$  [31].

Table III summarizes the lattice parameters, atomic positions, atomic moment of  $T$  site, relative total energies, and critical temperatures of  $T_2\text{AlB}_2$  with different magnetic configurations. The calculated lattice parameters and atomic positions agree well with experiments. The relaxed lattice parameters of  $T_2\text{AlB}_2$  not only vary with element  $T$  but also depend on the spin configuration. For  $\text{Fe}_2\text{AlB}_2$ , lattice parameters  $a$  and  $b$  decrease, and  $c$  increases when the spin configuration changes from NM  $\rightarrow$  AFM  $\rightarrow$  FM. The calculated lattice parameters using the FM configuration agree the best with experiments. For  $\text{Mn}_2\text{AlB}_2$ ,  $b$  and  $c$  increase when the spin configuration changes from NM  $\rightarrow$  FM  $\rightarrow$  AFM. Rel-

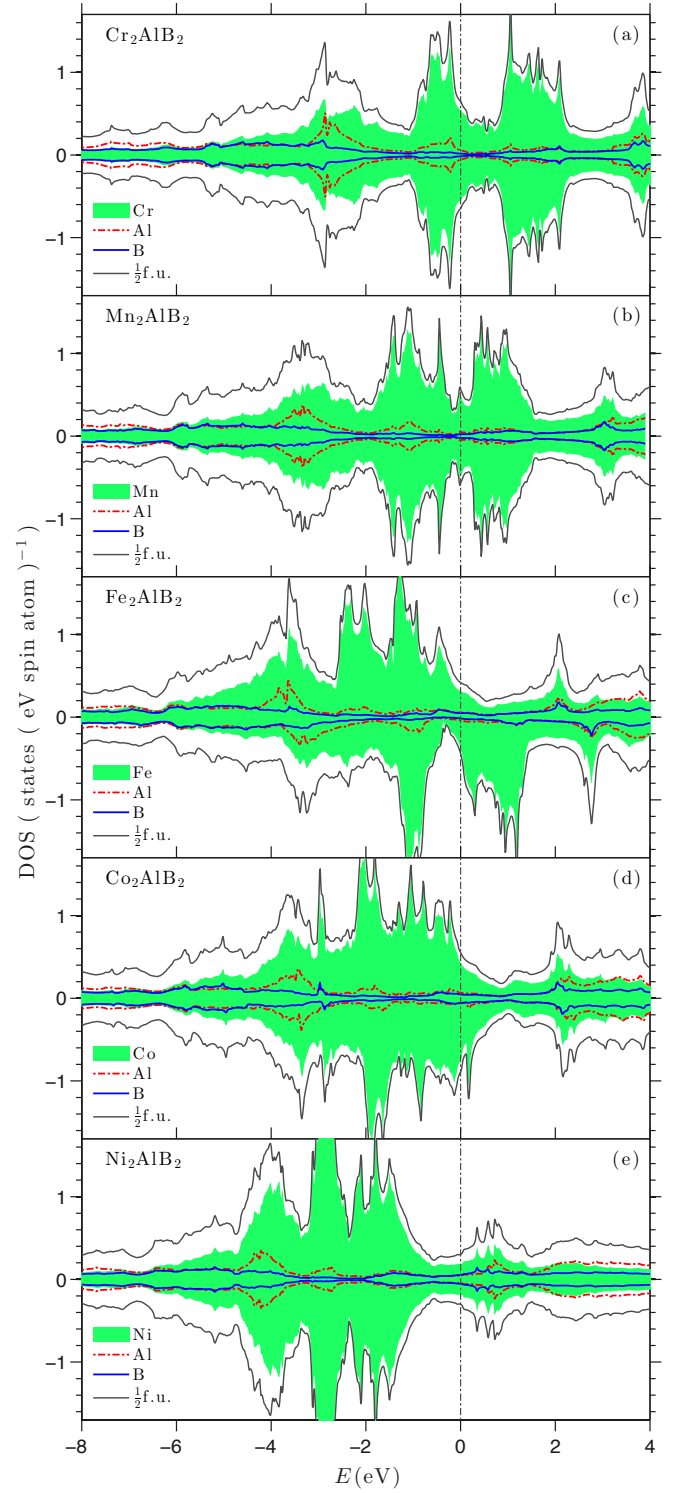


FIG. 4. Atom- and spin-projected, scalar-relativistic partial densities of states (DOS) in (a)  $\text{Cr}_2\text{AlB}_2$ , (b)  $\text{Mn}_2\text{AlB}_2$ , (c)  $\text{Fe}_2\text{AlB}_2$ , (d)  $\text{Co}_2\text{AlB}_2$ , and (e)  $\text{Ni}_2\text{AlB}_2$  calculated within GGA and using fully relaxed structures. The total DOS of the f.u. cell are scaled by  $\frac{1}{2}$  to better compare.  $\text{Cr}_2\text{AlB}_2$  and  $\text{Ni}_2\text{AlB}_2$  are nonmagnetic.  $\text{Mn}_2\text{AlB}_2$  is antiferromagnetic and  $\text{Fe}_2\text{AlB}_2$  is ferromagnetic.  $\text{Co}_2\text{AlB}_2$  is weakly ferromagnetic. Fermi energy  $E_F$  is at 0 eV.



TABLE III. Lattice parameters, internal atomic positions,  $y_{4j}$  and  $y_{4i}$ , on-site atomic magnetic moment of  $T$  atoms,  $m_T$  ( $\mu_B$ ), relative total energy (meV/f.u.), and critical temperatures (Curie temperature in  $\text{Fe}_2\text{AlB}_2$  or Néel temperature in  $\text{Mn}_2\text{AlB}_2$ ),  $T_C$  (K) in  $T_2\text{AlB}_2$  with  $T = \text{Fe}, \text{Mn}, \text{Cr}, \text{Co}$ , and  $\text{Ni}$ .  $T$  atom occupies the  $4j$  site ( $0 y_{4j} 1/2$ ) and B atom occupies the  $4i$  ( $0 y_{4i} 0$ ) site.

$T$	$a$	$b$	$c$	$y_{4j}$	$y_{4i}$	$m_T$	$\Delta E$	$T_C$
Cr	2.921	11.034	2.929	0.3521	0.2057	0		
Expt. [7]	2.937	11.07	2.971	0.352	0.220			
Expt. [32]	2.937	11.047	2.968					
Mn-NM	2.890	11.050	2.817	0.3562	0.2060	0	0	
Mn-FM	2.892	11.056	2.826	0.3551	0.2060	0.42	-21.5	
Mn-AFM	2.887	11.109	2.830	0.3547	0.2061	0.75	-63.6	296
Expt. [26]	2.92	11.08	2.89	0.355	0.209			
Expt. [9]	2.936	11.12	2.912					
Fe-NM	2.951	11.261	2.698	0.3531	0.2065	0	0	
Fe-AFM	2.941	11.212	2.739	0.3559	0.2070	1.06	-97.9	
Fe-FM	2.915	11.017	2.851	0.3537	0.2063	1.37	-164.1	298
Expt. [14]	2.923	11.034	2.870	0.3540	0.2071			
Co	2.962	11.314	2.689	0.3541	0.2073	0.21		
Ni	2.979	11.041	2.843	0.3586	0.2101	0		

ative to those of  $\text{Fe}_2\text{AlB}_2$ , the lattice parameter  $a$  of  $T_2\text{AlB}_2$  varies within  $0.06 \text{ \AA}$  (2.2%) in the sequence of  $\text{Mn} < \text{Fe} \approx \text{Cr} < \text{Co} < \text{Ni}$ ;  $b$  varies within  $0.30 \text{ \AA}$  (2.7%) in the sequence of  $\text{Fe} < \text{Ni} < \text{Cr} \approx \text{Mn} < \text{Co}$ ; and parameter  $c$  varies within  $0.16 \text{ \AA}$  (5.7%) in the sequence of  $\text{Co} < \text{Mn} < \text{Ni} \approx \text{Fe} < \text{Cr}$ . Percentagewise, the largest variation occurs with lattice parameter  $c$ . As we will show later,  $\text{Fe}_2\text{AlB}_2$  has a much stronger magnetoelastic effect along the  $c$  axis.

### B. Alloys: $M$ and $T_C$ in $\text{Fe}_{2-x}T_x\text{AlB}_2$

To investigate how magnetic properties change with the  $3d$  substitutions on Fe sites in  $\text{Fe}_2\text{AlB}_2$ , we first consider the chemical effect by neglecting the structure changes caused by substitution. The LMTO-ASA-CPA method is used to calculate the magnetization and the normalized effective exchange (or MFA estimation of  $T_C$  in units of pure  $\text{Fe}_2\text{AlB}_2$ ) in  $\text{Fe}_{2-x}T_x\text{AlB}_2$  as functions of doping concentration  $x$ , with  $T = \text{Cr}, \text{Mn}, \text{Co}$ , and  $\text{Ni}$ . The experimental lattice parameters and atomic positions of  $\text{Fe}_2\text{AlB}_2$  are used and the results are shown in Fig. 5. All dopings decrease the magnetization and  $T_C$  in  $\text{Fe}_2\text{AlB}_2$ . The component-resolved atomic spin moments in those alloys are shown in Fig. 6. For Mn doping, we also consider the AFM configuration and show the absolute values of component-resolved moments in Fig. 6(b).

Assuming the FM configuration, Mn has the slightest effect on the decrease of the magnetization and  $T_C$ . The Fe moment barely changes and even increases with a higher Mn content. The decrease of total magnetiza-

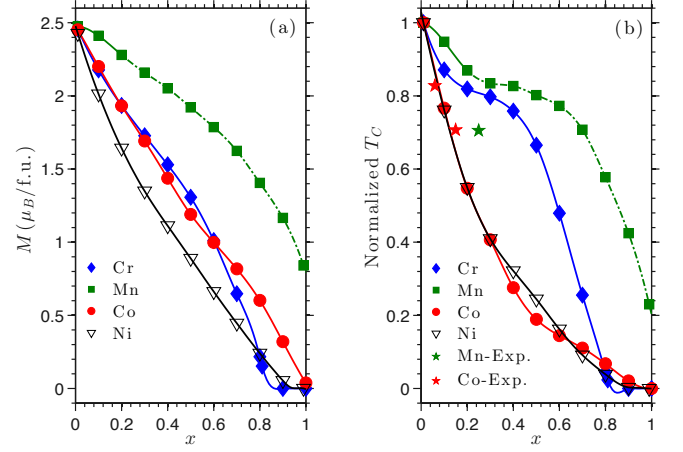


FIG. 5. Spin magnetization  $M$  (a) and normalized  $T_C$  (b) as functions of doping concentration  $x$  in  $(\text{Fe}_{1-x}T_x)_2\text{AlB}_2$  with  $T = \text{Cr}, \text{Mn}, \text{Co}$ , and  $\text{Ni}$ . Theoretical  $T_C$  is estimated within MFA and normalized with respect to pure  $\text{Fe}_2\text{AlB}_2$ . Experimental  $T_C$  values of Mn and Co, adopted from Refs.[5] and [10], are denoted by stars in green and red, respectively. For  $(\text{Fe}_{1-x}\text{Mn}_x)_2\text{AlB}_2$ , the FM configuration becomes less stable than AFM within CPA after  $x > 0.2$ , which are denoted by the green dashed line.

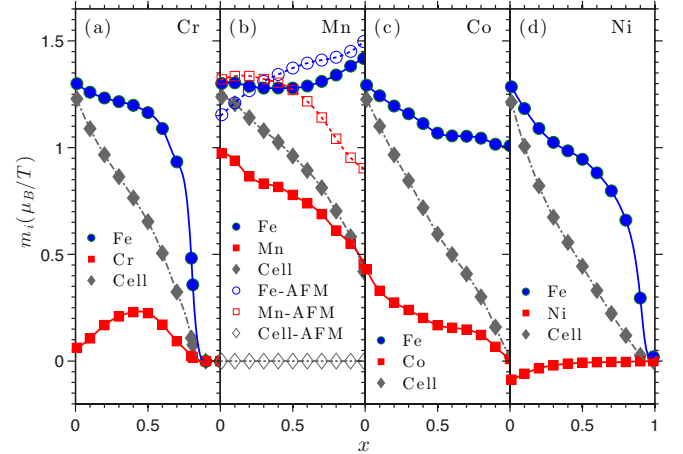


FIG. 6. Component-resolved atomic spin moments  $m_i$  as functions of doping content  $x$  in  $\text{Fe}_{2-x}T_x\text{AlB}_2$  with  $T = \text{Cr}$  (a),  $\text{Mn}$  (b),  $\text{Co}$  (c), and  $\text{Ni}$  (d). Calculations are carried out using the LMTO-ASA-CPA method. Structural changes due to substitution are neglected, and the experimental lattice parameters and atomic positions of  $\text{Fe}_2\text{AlB}_2$  are used for all calculations. For  $T = \text{Mn}$ , the AFM configuration is also considered besides the FM configuration, and the absolute magnetic moments of Mn and Fe components are shown.

tion is due to the dilution of Fe moments with smaller Mn moments. With a 25% Mn content, the calculated  $T_C$  decreases by 20% while experiments found a larger  $\Delta T_C = -30\%$ . The assumption of FM configuration is logical when the Mn amount is small. However, at a higher Mn content, the AFM configuration should also be considered, given that pure  $\text{Mn}_2\text{AlB}_2$  is more stable with

the AFM configuration. Here we calculate the AFM configuration in CPA, by assuming the spin moments of 3d atoms (both Fe and Mn components) are parallel within the  $ab$  plane and antiparallel between neighboring planes. As shown in Fig. 6(b), in comparison with the FM configuration, the AFM configuration gives larger Mn moments in the whole doping range and larger Fe moments at  $x \geq 0.3$ . Within CPA and without considering any lattice relaxation, the AFM configuration becomes more stable than the FM configuration with  $x > 0.2$ . Thus, the larger decrease of  $T_C$  observed in experiments is likely caused by the forming of AFM phases in the samples. By systematically investigating solid solutions  $(\text{Fe}_{1-x}\text{Mn}_x)_2\text{AlB}_2$ , Chai *et al.* observed both NM and FM Mössbauer spectral components in all Mn-containing samples and attributed them to the clustering of Mn-rich and Fe-rich regions in the samples. Moreover, a spin-glass state has been observed at low temperature in  $(\text{Fe}_{1-x}\text{Mn}_x)_2\text{AlB}_2$  with  $x = 0.25$  and this phenomenon had been interpreted as the result of geometric frustration caused by the triangular configuration of magnetic atoms [5]. Here, we argue that it could be caused by the competition between the FM and AFM configurations along the  $c$  axis.

Given that a large DOS lies right above the Fermi level in the minority spin channel as shown in Fig. 4(c), it is not surprising that the electron doping, such as Co or Ni doping, decreases the magnetic moment on Fe sites. With a small amount of Co doping, the magnetization and  $T_C$  decrease nearly linearly with Co content. Similar linear dependence of  $T_C$  on Co content had been observed in experiments. As shown in Fig. 5(b), calculated  $\Delta T_C$  values agree very well with experiments [10]. With  $0.4 < x < 0.9$ , Co atoms in  $(\text{Fe}_{1-x}\text{Co}_x)_2\text{AlB}_2$  have a small moment of  $\sim 0.2 \mu_B/\text{Co}$ , similar to the Co moment calculated in the fully relaxed structure of  $\text{Co}_2\text{AlB}_2$  using FP. However, this small moment becomes unstable in ASA at  $x = 1$ .

In comparison to Co doping, Ni doping has a similar effect on decreasing  $T_C$  and an even stronger effect on suppressing the magnetization in  $\text{Fe}_2\text{AlB}_2$ . As shown in Fig. 6(d), the atomic Ni moment in  $(\text{Fe}_{1-x}\text{Ni}_x)_2\text{AlB}_2$  is small and coupled antiparallel with the Fe sublattice at small  $x$ , and negligible for  $x > 0.3$ .

In  $(\text{Fe}_{1-x}\text{Cr}_x)_2\text{AlB}_2$ , the Cr moment is small and parallel to the Fe sublattice. The maximum Cr moment of  $0.2 \mu_B/\text{Cr}$  occurs at  $x = 0.5$ . Like Mn, Cr doping has a smaller effect on decreasing the  $T_C$  than Co and Ni. However, Cr doping is not likely to promote the FM  $\rightarrow$  AFM transition, which may compromise the MCE as in the case of Mn doping [5]. Thus, it is worthwhile to investigate Cr doping, which may provide a useful approach to tune the  $T_C$  and MCE in  $\text{Fe}_2\text{AlB}_2$ .

### C. Effect of lattice distortion

Besides the chemical effect, the volume change caused by substitution may also affect the magnetic properties.

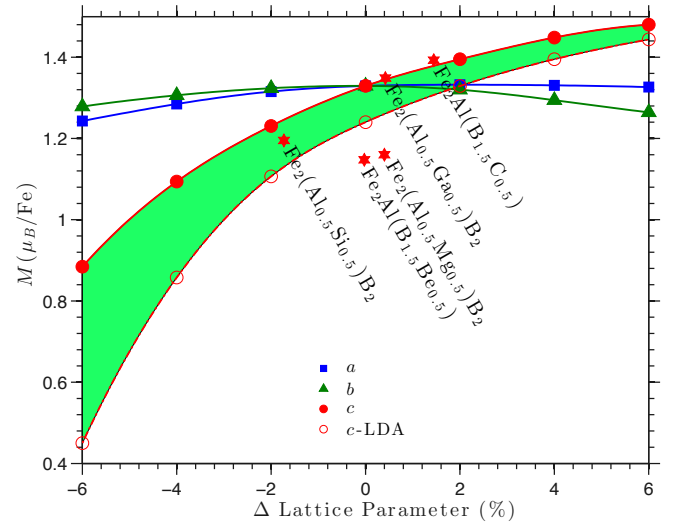


FIG. 7. Magnetization as functions of lattice parameters. Each of the three lattice parameters is varied with the other two being preserved. For the lattice distortion along the  $c$  axis, LDA results are also shown to compare. Magnetizations calculated in fully relaxed  $\text{Fe}_2\text{Al}(\text{B}_{1.5}\text{Be}_{0.5})\text{B}_2$ ,  $\text{Fe}_2\text{Al}(\text{B}_{1.5}\text{Co}_{0.5})\text{B}_2$ ,  $\text{Fe}_2(\text{Al}_{0.5}\text{Mg}_{0.5})\text{B}_2$ ,  $\text{Fe}_2(\text{Al}_{0.5}\text{Si}_{0.5})\text{B}_2$ , and  $\text{Fe}_2(\text{Al}_{0.5}\text{Ga}_{0.5})\text{B}_2$  are also shown.

As shown in Table III, the lattice parameters in  $\text{Fe}_2\text{AlB}_2$  vary with the element  $T$  and spin configuration. To have a rough idea on the magnetoelastic effect in  $\text{Fe}_2\text{AlB}_2$ , we calculate the magnetization dependence on the three lattice parameters, respectively. Starting from the fully relaxed structure, each of the three parameters is varied while the other two are kept constant. Interestingly, as shown in Fig. 7, the magnetoelastic effect in  $\text{Fe}_2\text{AlB}_2$  is very anisotropic. The magnetization has a much stronger dependence on the lattice parameter  $c$  than on  $a$  or  $b$ . With  $\Delta c = -6\%$ , magnetization decreases by 35% within GGA and 60% within LDA.

This anisotropic magnetoelastic effect can be understood by investigating the electronic structure features near  $E_F$  and their changes caused by the lattice distortion. The band structures of  $\text{Fe}_2\text{AlB}_2$  in the majority and minority channels are shown in Fig. 8(a, c), respectively. The PDOS projected on Fe-3d states and in two spin channels are shown in Fig. 8(b). Particularly of note is a narrow band right above  $E_F$  in the minority spin channel. This band is found to consist almost entirely of Fe- $d_{xy}$  and  $d_{x^2-y^2}$  ( $m = \pm 2$ ) orbitals. The variations of PDOS with lattice parameter  $c$  are shown in Fig. 9. The decreasing of parameter  $c$  increases the bandwidth of the  $d_{3z^2-1}$  state, which has a relatively large density right below  $E_F$  in the majority spin channel. These anti-bonding  $d_{3z^2-1}$  states, located between  $-1.3 \text{ eV}$  and  $E_F$ , shift up toward  $E_F$  and become less occupied. Correspondingly, the aforementioned peak of  $m = \pm 2$  states, located right above  $E_F$  in the minority spin channel, become more occupied. As a result, the magnetization decreases. The Fe- $d_{yz}$  and  $d_{xz}$  states ( $m = \pm 1$ ) have small

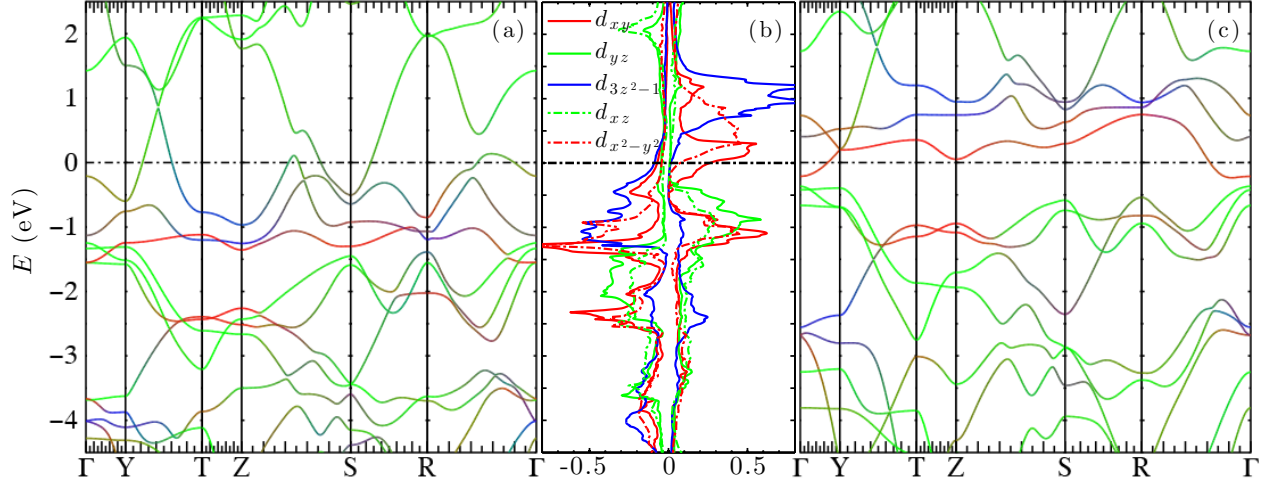


FIG. 8. Band structure of  $\text{Fe}_2\text{AlB}_2$  in (a) majority and (c) minority spin channels. Bands are with color weights, with blue identifying the  $\text{Fe-}d_{3z^2-1}$  states, red the  $\text{Fe-}(d_{xy}, d_{x^2-y^2})$  states, and green everything else. PDOS [states (eV spin atom) $^{-1}$ ] projected on Fe-3d states in two spin channels are shown in panel (b). The left and right portions of panel (b) show PDOS in the majority and minority spin channels, respectively. The horizontal dashed lines in all three panels indicate the Fermi level.

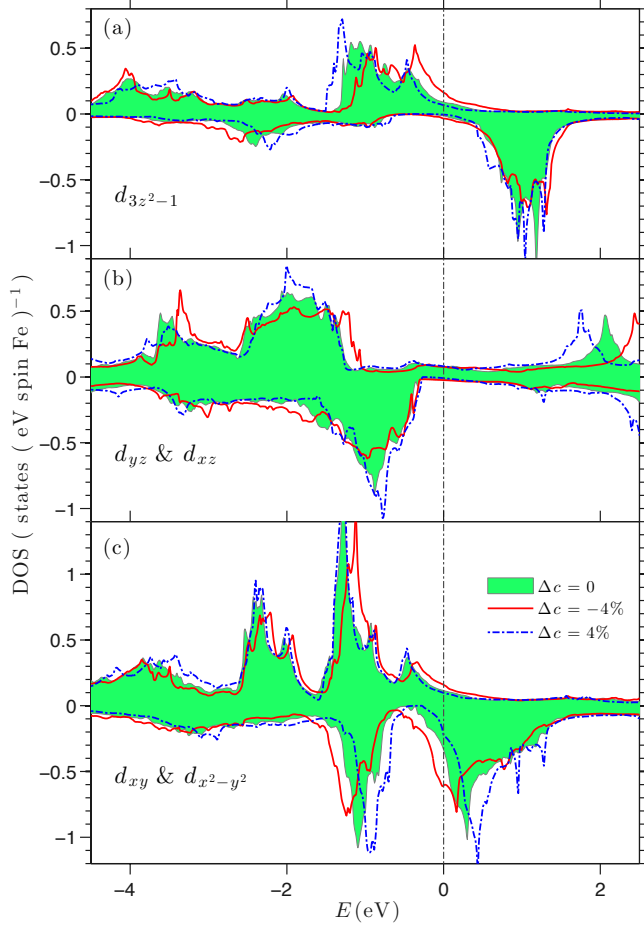


FIG. 9. The partial density of states projected on Fe 3d with different  $c$  parameters. The scalar-relativistic partial density of states projected on the 3d states of Fe sites in  $\text{Fe}_2\text{AlB}_2$  with different lattice parameters.

DOS around  $E_F$  and contribute less to this magnetization change. With the further decrease of  $c$  and then magnetization, the spin splitting becomes smaller, which quickly accelerates the decrease of magnetization as  $\Delta c$  approaches to  $-6\%$ .

#### D. Dopings on B and Al sites

We also consider the substitutions of B and Al atoms with their neighboring elements in the periodic table: Be and C atoms on the B site, and Mg, Si, and Ga atoms on the Al site. The stabilities of those dopings are not well understood, and a careful and complete future investigation is desired. Here we focus on the possible effects of those dopings on the magnetization. Using various configurations of a ten-atom  $\text{Fe}_2\text{AlB}_2$  unit cell, we substitute one B or Al atom with a dopant atom and fully relax the structures for  $\text{Fe}_2\text{Al}(\text{B}_{0.75}\text{Z}_{0.25})_2$  with  $\text{Z} = \text{Be}$  and  $\text{C}$ , and  $\text{Fe}_2(\text{Al}_{0.5}\text{Z}_{0.5})\text{B}_2$  with  $\text{Z} = \text{Mg}$ ,  $\text{Si}$ , and  $\text{Ga}$ . Their magnetizations calculated with the corresponding lowest energy configuration are denoted in Fig. 7 with respect to the change of lattice parameter  $c$ .

Only C doping on the B sites noticeably increases the lattice parameter  $c$  and magnetization, while most other substitutions decrease the magnetization in  $\text{Fe}_2\text{AlB}_2$ . Both chemical effect and the magnetoelastic effect contribute to the magnetization enhancement. The lattice parameter  $c$  increases by 1.6% and magnetization increases to  $1.4\mu_B/\text{Fe}$  in  $\text{Fe}_2\text{Al}(\text{B}_{0.75}\text{C}_{0.25})_2$ . Unlike B, C has a small moment parallel to the Fe sublattice. Moreover, C doping increases the moments of neighboring Fe atoms by about  $0.1\mu_B/\text{Fe}$ .

For Si doping, without considering lattice relaxation, magnetization decreases by 6% in  $\text{Fe}_2(\text{Si}_{0.5}\text{Al}_{0.5})\text{B}$ . The



relaxation decreases the lattice  $c$  by 1.7%, and further decreases the magnetization by another 6%. Thus, both chemical effect and the magnetoelastic effect contribute to the decreasing of the magnetization. Be and Mg dopings have stronger effects on decreasing the magnetization. With Be and Mg dopings, the DOS peak right below  $E_F$  in the majority spin shifts toward  $E_F$  and becomes less occupied and the magnetization decreases to about  $1.1 \mu_B/\text{Fe}$ . Ga doping has very small effect on the lattice parameters and the magnetization of  $\text{Fe}_2\text{AlB}_2$ .

#### IV. CONCLUSION

Using density functional theory, we investigated the intrinsic magnetic properties in  $T_2\text{AlB}_2$  and their alloys. For  $\text{Fe}_2\text{AlB}_2$ , the  $a$  axis is the easiest axis, while the  $c$  axis is the hardest axis. For  $\text{Mn}_2\text{AlB}_2$ , we predict that the magnetic ground state is an AFM configuration, with the neighboring Mn layers being antiferromagnetically coupled along the  $c$  axis.  $\text{Co}_2\text{AlB}_2$  is weakly ferromagnetic, while  $\text{Cr}_2\text{AlB}_2$  and  $\text{Ni}_2\text{AlB}_2$  are nonmagnetic. All  $3d$  substitutions decrease the magnetization and Curie temperature of  $\text{Fe}_2\text{AlB}_2$  in the sequence of  $\text{Mn} < \text{Cr} < \text{Co} < \text{Ni}$ . However, Mn promotes antiferromagnetism when its doping content is larger than 20%. The competition between the two configurations at crit-

ical compositions may be responsible for the spin-glass states observed in experiments. Unlike Mn, Cr doping is not likely to promote the AFM configuration, and may be useful in tuning  $T_C$  in  $\text{Fe}_2\text{AlB}_2$ . The effects of strain and alloying on magnetic properties are also studied. A very strong anisotropic magnetoelastic effect is found. Magnetization in  $\text{Fe}_2\text{AlB}_2$  becomes fragile and quickly decreases with the lattice parameter  $c$ , while it barely changes with  $a$  and  $b$ . This effect is explained by the displacement of antibonding  $d_{3z^2-1}$  states right below the Fermi level in the majority spin channel, and the filling of unoccupied  $d_{xy}$  and  $d_{x^2-y^2}$  states which have a sharp peak right above the Fermi level in the minority spin channel. Doping or applying pressure to modify the interlayer distance along the  $c$  axis may provide an effective way to tune the magnetic properties in  $\text{Fe}_2\text{AlB}_2$ .

#### V. ACKNOWLEDGMENTS

We thank R. W. McCallum, L. Lewis, R. Barua, and B. Jensen for helpful discussions. Work at Ames Laboratory was supported by the U.S. Department of Energy, Advanced Research Projects Agency-Energy (ARPA-E) under Grant No. 1002-2147. Ames Laboratory is operated for the U.S. Department of Energy by Iowa State University under Contract No. DE-AC02-07CH11358.

- 
- [1] V. K. Pecharsky and K. A. Gschneidner, Jr., *Phys. Rev. Lett.* **78**, 4494 (1997).
  - [2] X. Tan, P. Chai, C. M. Thompson, and M. Shatruk, *Journal of the American Chemical Society* **135**, 9553 (2013).
  - [3] L. Lewis, R. Barua, and B. Lejeune, *Journal of Alloys and Compounds* **650**, 482 (2015).
  - [4] Q. Du, G. Chen, W. Yang, Z. Song, M. Hua, H. Du, C. Wang, S. Liu, J. Han, Y. Zhang, and J. Yang, *Japanese Journal of Applied Physics* **54**, 053003 (2015).
  - [5] Q. Du, G. Chen, W. Yang, J. Wei, M. Hua, H. Du, C. Wang, S. Liu, J. Han, Y. Zhang, and J. Yang, *Journal of Physics D: Applied Physics* **48**, 335001 (2015).
  - [6] H. J. Becher, K. Krogmann, and E. Peisker, *Z. Anorg. Allg. Chem.* **344**, 140 (1966).
  - [7] N. Chaban and Y. Kuz'ma, *Inorg. Mater.* **9**, 1696 (1973).
  - [8] K. Kádas, D. Iuşan, J. Hellsvik, J. Cedervall, P. Berastegui, M. Sahlberg, U. Jansson, and O. Eriksson, *Journal of Physics: Condensed Matter* **29**, 155402 (2017).
  - [9] P. Chai, S. A. Stoian, X. Tan, P. A. Dube, and M. Shatruk, *Journal of Solid State Chemistry* **224**, 52 (2015), chemistry of two-dimensional materials.
  - [10] S. Hirt, F. Yuan, Y. Mozharivskyj, and H. Hillebrecht, *Inorganic Chemistry* **55**, 9677 (2016).
  - [11] M. ElMassalami, D. da S. Oliveira, and H. Takeya, *Journal of Magnetism and Magnetic Materials* **323**, 2133 (2011).
  - [12] Y. Cheng, Z. Lv, X. Chen, and L. Cai, *Computational Materials Science* **92**, 253 (2014).
  - [13] J. Cedervall, M. S. Andersson, T. Sarkar, E. K. Delczeg-Czirjak, L. Bergqvist, T. C. Hansen, P. Beran, P. Nordblad, and M. Sahlberg, *Journal of Alloys and Compounds* **664**, 784 (2016).
  - [14] W. Jeitschko, *Acta Crystallographica Sect. B: Struct. Sci., Cryst. Eng. Mater.* **25**, 163 (1969).
  - [15] O. Andersen, *Phys. Rev. B* **12**, 3060 (1975).
  - [16] M. Methfessel, M. van Schilfgaarde, and R. Casali, in *Lecture Notes in Physics*, Vol. 535, edited by H. Dreyse (Springer-Verlag, Berlin, 2000).
  - [17] J. P. Perdew, K. Burke, and M. Ernzerhof, *Phys. Rev. Lett.* **77**, 3865 (1996).
  - [18] U. von Barth and L. Hedin, *Journal of Physics C: Solid State Physics* **5**, 1629 (1972).
  - [19] A. Mackintosh and O. Andersen, *Electrons at the Fermi Surface* (Cambridge University Press, Cambridge, England, 1980).
  - [20] L. Ke, M. van Schilfgaarde, and V. Antropov, *Phys. Rev. B* **86**, 020402 (2012).
  - [21] L. Ke, K. Belashchenko, M. van Schilfgaarde, T. Kotani, and V. Antropov, *Phys. Rev. B* **88**, 024404 (2013).
  - [22] L. Ke and D. D. Johnson, *Phys. Rev. B* **94**, 024423 (2016).
  - [23] G. Kresse and J. Hafner, *Phys. Rev. B* **47**, 558 (1993).
  - [24] G. Kresse and J. Furthmüller, *Phys. Rev. B* **54**, 11169 (1996).
  - [25] G. Kresse and D. Joubert, *Phys. Rev. B* **59**, 1758 (1999).
  - [26] K. Cenxual, L. M. Gelato, M. Penzo, and E. Parthé, *Acta Crystallographica Sect. B: Struct. Sci., Cryst. Eng. Mater.* **47**, 433 (1991).

- [27] V. Antropov, L. Ke, and D. Åberg, Solid State Communications **194**, 35 (2014).
- [28] L. Ke and M. van Schilfgaarde, Phys. Rev. B **92**, 014423 (2015).
- [29] L. Ke, D. A. Kukusta, and D. D. Johnson, Phys. Rev. B **94**, 144429 (2016).
- [30] P. Bruno, Phys. Rev. B **39**, 865 (1989).
- [31] A. V. D. Geest and A. Kolmogorov, Calphad **46**, 184 (2014).
- [32] J. Lu, S. Kota, M. W. Barsoum, and L. Hultman, Materials Research Letters **0**, 1 (2016).